

Using time-resolved penumbral imaging to measure low hot spot x-ray emission signals from capsule implosions at the National Ignition Facility^{a)}

D.T. Bishel,¹ B. Bachmann,¹ A. Yi,² D. Kraus,³ L. Divol,¹ M. Bethkenhagen,^{1,4} R.W. Falcone,⁵ L.B. Fletcher,⁶ S.H. Glenzer,⁶ O.L. Landen,¹ M.J. MacDonald,⁵ N. Masters,¹ P. Neumayer,⁷ R. Redmer,⁴ A.M. Saunders,⁵ B. Witte,^{4,6} and T. Döppner^{1,*}

¹⁾Lawrence Livermore National Laboratory, Livermore 94550, USA

²⁾Los Alamos National Laboratory, Los Alamos, New Mexico 87545, USA

³⁾Helmholtz-Zentrum Dresden-Rossendorf, 01328 Dresden, Germany

⁴⁾Institut für Physik, Universität Rostock, 18051 Rostock, Germany

⁵⁾Department of Physics, University of California, Berkeley, California 94720, USA

⁶⁾SLAC National Accelerator Laboratory, Menlo Park, California 94720, USA

⁷⁾GSI Helmholtzzentrum für Schwerionenforschung, 64291 Darmstadt, Germany

(Dated: 17 July 2018)

We have developed and fielded a new x-ray pinhole-imaging snout that exploits time-resolved penumbral imaging of low-emission hot spots in capsule implosion experiments at the National Ignition Facility (NIF). We report on results for a series of indirectly driven Be capsule implosions that aim at measuring x-ray Thomson scattering (XRTS) spectra at extreme density conditions near stagnation. In these implosions, x-ray emission at stagnation is reduced by 100 – 1000x compared to standard inertial confinement fusion (ICF) implosions to mitigate undesired continuum background in the XRTS spectra. Our snout design enables not only measurements of peak x-ray emission times, t_o , where standard ICF diagnostics would not record any signal, but also allows for inference of hot spots shapes. Measurement of t_o is crucial to account for shot-to-shot variations in implosion velocity and therefore to benchmark the achieved plasma conditions between shots and against radiation hydrodynamics simulations. Additionally, we used differential filtering to infer a hot spot temperature of 520 ± 80 eV, which is in good agreement with predictions from radiation hydrodynamic simulations. We find that, despite fluctuations of the x-ray flash intensity of up to 5x, the emission time history is similar from shot to shot, and slightly asymmetric with respect to peak x-ray emission.

I. INTRODUCTION

In recent years, large-scale high-energy laser facilities like the National Ignition Facility (NIF)¹, built for the quest to demonstrate controlled inertial confinement fusion², have enabled the creation of high-energy-density plasmas (HEDP) in the laboratory at conditions relevant to astrophysical bodies.^{3–5} Characterizing the plasma conditions at such extreme conditions is crucial to test and benchmark state-of-the-art HEDP models. X-ray Thomson scattering (XRTS) has emerged as a particularly useful diagnostic technique, as both the electron temperature and electron density can be inferred from a single spectrum.⁶ We have developed an experimental platform at the NIF to measure XRTS spectra from matter at extreme compressions present near stagnation in indirectly-driven capsule implosions (cf. Fig. 1).^{7–9} In this paper, we present a novel penumbral imaging snout that measures the spatially- and temporally-resolved hot spot emission of the stagnating capsule from the polar view. As such, it is a key element of our XRTS platform because it (i) provides a timing fiducial to correct for

shot-to-shot fluctuations in our implosion experiments, (ii) monitors and confirms the roundness of the hot spot, and (iii) enables inference of the hot spot temperature from the signal ratio of differentially filtered images.

Even for nominally identical experiments, the capsule trajectory and thus the time of stagnation can vary by several 100 ps due to variations in capsule parameters like capsule thickness and impurity/ dopant fractions, and due to variations in laser delivery. These shot-to-shot variations complicate any direct comparison of plasma and capsule parameters between shots, which include XRTS measurements and dedicated in-flight radiography measurements of the capsule trajectory. To account for shot-to-shot variations in capsule trajectory, we exploit the x-ray emission from the hot spot formed at stagnation as a timing fiducial, enabling a more informative comparison between experiments. In these implosions, x-ray emission at stagnation is intentionally reduced by 100 – 1000x compared to standard inertial confinement fusion (ICF) implosions to mitigate undesired continuum background in the XRTS spectra. This is achieved by operating at reduced implosion velocity (~ 200 km/s) and lower capsule gas fill, resulting in reduced hot spot temperature and volume compared to typical ICF implosions. Though highly sophisticated x-ray hot spot diagnostics have been developed for ICF implosion experiments at the NIF, these are insufficient for measuring the low hot spot x-ray emission signals present in experiments using our XRTS capsule implosion platform (cf. Fig. 1a).⁷

^{a)}Contributed paper published as part of the Proceedings of the 22nd Topical Conference on High-Temperature Plasma Diagnostics, San Diego, California, April, 2018;

^{*}Corresponding author: doepner1@llnl.gov

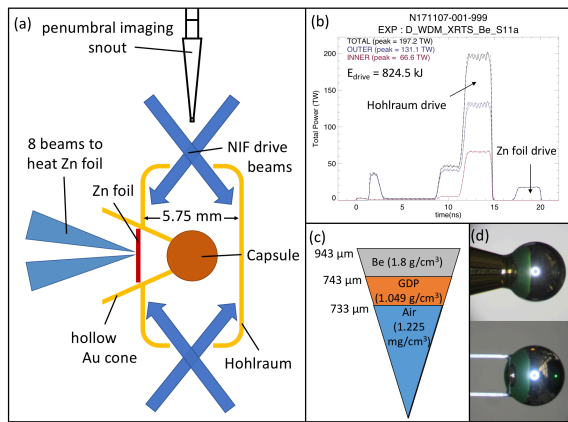


FIG. 1. (a) Experimental platform for XRTS measurements⁷, shown for a Au cone supported capsule. For details on the snout, see Figure 2. (b) Requested and delivered laser drive; for details, see text. (c) Schematic of nominal Be capsule. (d) Photographs of as-built capsules with Au cone (top) and HDC stalk (bottom) supports.

To compensate for the decrease in x-ray emission from the stagnated core, we have developed and fielded a new pinhole-imaging snout (cf. Fig. 2) that employs time-resolved penumbral imaging.^{10–12}

Before we describe details of the new penumbral imaging snout in Section III, we introduce the experimental campaign for which the diagnostic was developed (Section II). In Section IV we present the results of recent experiments that fielded the diagnostic, demonstrate the use of hot spot x-ray emission as a time fiducial, and compare the experimentally derived plasma temperature and core size to hydrodynamic simulations. Conclusions and final statements are included in Section V.

II. EXPERIMENTAL PLATFORM

The new penumbral imaging snout has been fielded on indirect-drive capsule implosions at the NIF that seek to collect XRTS signals from CH and Be at high density ($n_e \approx 10^{25} \text{ cm}^{-3}$), cf. Fig. 1.⁷ In this paper, we present results for a series of Be capsule implosions. The un-doped Be capsules are 200 μm -thick, and were coated onto a 10 μm -thick plastic layer (glow discharge polymer (GDP))¹³, cf. Fig. 1(c). They are filled with air at ambient pressure. Since mid- and high-Z impurities complicate the interpretation of the XRTS measurement¹⁴, the capsules were kept closed (no fill-tube hole drilled) and were not heated to high temperatures to avoid additional oxygen uptake in the Be capsule, consequentially leaving the plastic mandrels intact and unmelted inside the capsules. Likewise, we did not use Ar-assisted coating to minimize the amount of Ar in the capsule. The experiments are fielded at room-temperature in scale575 Au hohlraums filled with Neopentane (C_5H_{12}) at 1.37 mg/cm^3 . 184 NIF beams were used to produce the soft

x-ray hohlraum drive (cf. Fig. 1(b)), which is derived from ICF tuning experiments.¹⁵ Peak power is reduced to 200 TW, and the drive is truncated at a total laser energy of 825 kJ, resulting in a peak radiation temperature of 230 eV. Cross beam energy transfer from the outer to the inner (23° and 30°) laser cones by setting the wavelength separation to $\Delta\lambda_{30/23} = 5.7/6.4 \text{ \AA}$ is used to control implosion symmetry.

Eight laser beams are reserved for heating a Zn foil attached to the outside of the hohlraum to produce He_α x-rays at 9.0 keV that scatter off the imploding capsule. The scattered x-rays are collected by the Mono-Angle Crystal Spectrometer (MACS)⁹ through a diagnostic window towards target chamber coordinates (90-68). There is an additional diamond hohlraum window opposite to the diagnostic port (towards 90-248) to reduce wall emission background seen by the XRTS spectrometer. The Zn foil is enclosed by an external Au shield to block the direct line-of-sight of the exploding Zn foil to the MACS spectrometer. The azimuthal location of the cone and the Zn foil determines the scattering angle. To date, we have fielded XRTS measurements with scattering angles ranging from 45° to 120° . For the larger angles, the capsule is held by an inner Au cone (cf. Fig. 1d, top), which also serves as a collimator for the Zn He_α x-ray source. This experimental target design was inspired by the hydrogrowth-radiography (HGR) platform, which explored cone-mounted capsules in detail.^{16,17} For scattering angles of 45° and smaller, the use of an inner Au cone is not viable because its tip would have a direct line-of-sight to the XRTS spectrometer, which could result in recording x-ray scattering from the Au cone tip and possibly thermal and line emission from the heated Au cone. Therefore, in experiments operating at small scattering angles, we have shortened the inner cone and hold the Be capsule by two high-density carbon (HDC) stalks (cf. Fig. 1(d), bottom). This stalk support scheme uses two 0.085 mm square, 1.7 mm long HDC stalks to suspend the capsule within the hohlraum. The slender, low-Z stalks produce negligible x-ray emission in our spectral region of interest.

III. PENUMBRA IMAGING

A schematic of the penumbral imaging snout assembly is shown in Figure 2. The nose cone of the snout is outfitted with a standard collimator that serves as an array of large-diameter ($d = 150 \mu\text{m}$) pinholes (cf. Fig. 2(b)), increasing throughput by a factor of 100 over the more common $\sim 10 \mu\text{m}$ pinholes.^{10,11} Since the pinholes are larger than the hot spot diameter, the hot spot shape information is encoded in the penumbra. Constructed from 500 μm thick Ta, the collimator mask stands 95 mm from target chamber center (TCC) to provide a 13x magnification. Each penumbral aperture is checked for circularity and deviates negligibly from round ($< 5.0\%$ on average). The resulting penumbral images are ana-

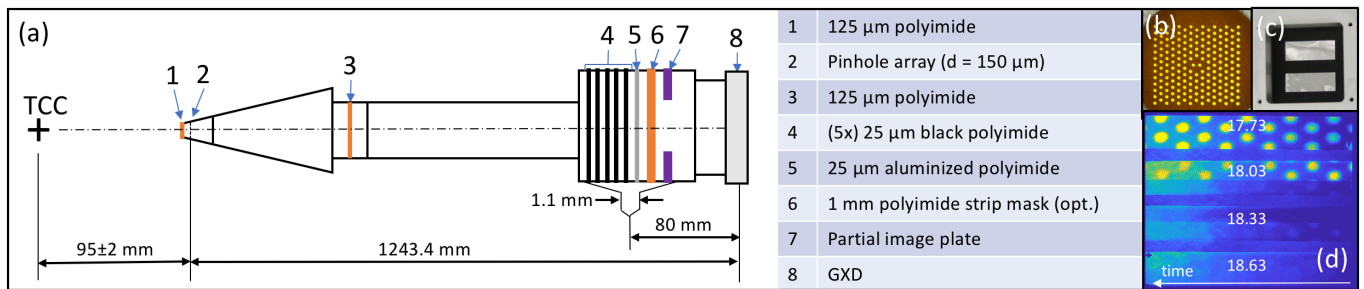


FIG. 2. (a) Schematic of penumbral imaging snout. Filtering elements are listed in the adjoined table. Note that the filtering stack (4 through 7) is assembled without any separation between its elements. The image plate (7) records time-integrated emission around the GXD for photometric calculations. (b) Photograph of the pinhole array (1 and 2). (c) View from the rear of the snout. The strip mask is visible in black. (d) Raw data from N160801-001. The time in nanoseconds corresponding to the central pixel of each strip is shown. The time at which each pixel is recorded increases from right to left. The strip mask runs horizontally across the center of the image, filtering half of each of the two center strips.

lyzed and reconstructions are performed as described in Ref. 11. The pinhole images are attenuated by multiple polyimide filters with 400 μm total thickness, and then projected onto the Gated X-ray Detector (GXD)^{18,19}, a 4-strip variable delay framing camera fiber-coupled to a CCD, which is mounted behind the snout assembly. Each strip is streaked in time over 240 ps with an integration time of $100 \pm 5 \text{ ps}$ ²⁰. As a result, each pinhole image is recorded at a different time during the implosion. Representative raw data is shown in Figure 2(d).

The filtering is significantly reduced compared to standard pinhole imaging snouts in order to increase signal by five- to ten-fold while still shielding the detector from debris ejected from the laser-target interaction. The final stage of polyimide filters consists of six 25 μm layers because this is thought to provide better protection against projectiles than a single 150 μm filter. An optional 1 mm differentially filtering polyimide strip mask (cf. Fig. 2(c)) is also available. When included, this filter covers half of each of the two center strips, and allows inference of the radiation temperature of the hot spot from the ratio between the filtered and unfiltered signals.²¹

TABLE I. Values used to align emission data. Δt is the delay of t_0 with respect to reference shot N160801-001. For a decrease in the micro-channel plate bias voltage of 20 V, the gain is expected to increase by a factor of $3^{\frac{20V}{50V}} \approx 1.55$; this relative gain is accounted for in the displayed amplitudes.

Shot	t_0 (ns)	Δt (ns)	Amplitude (a.u.)	Bias (V)
N160801-001	17.88	0.00	2.5	200
N170214-001	17.91	0.03	4.6	200
N170215-001	18.13	0.25	1.0	200
N171107-001	17.98	0.10	3.7	220
N171108-002	18.13	0.25	1.9	220

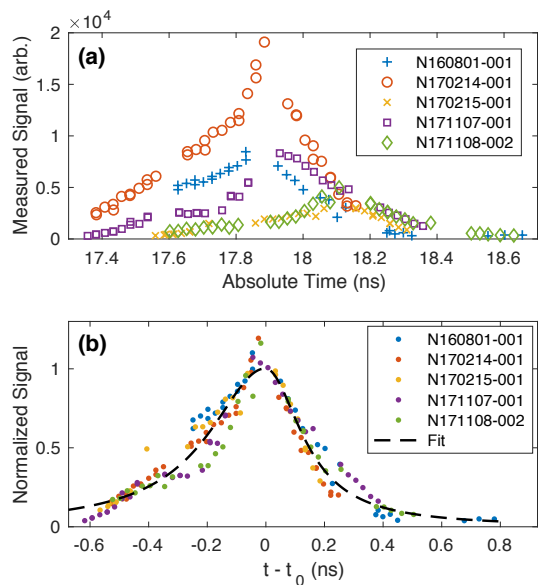


FIG. 3. (a) Temporal hot spot x-ray emission profiles for multiple shots. Each data point is taken from a different pinhole image. Peak emission time, t_0 of each shot is inferred from the corresponding dataset. (b) Normalized emission against time from t_0 . The dashed line is a fit to the two-sided Lorentzian of Equation (1) for all of the data shown. From the fit we measure $\Gamma_l = 0.47 \pm 0.04 \text{ ns}$ and $\Gamma_r = 0.30 \pm 0.03 \text{ ns}$.

IV. RESULTS AND DISCUSSION

From the penumbral images of the hot spot recorded by the GXD, we can track x-ray emission in time and thus identify the time of peak x-ray emission t_0 for each shot (cf. Fig. 3(a)). These data contain emission measurements from both gold cone and HDC stalk supported capsules. We use “flat-field” measurements to correct for differences in gain along a given strip (voltage droop) and between strips. When plotting flat-field corrected emission versus time from t_0 and normalizing to the in-

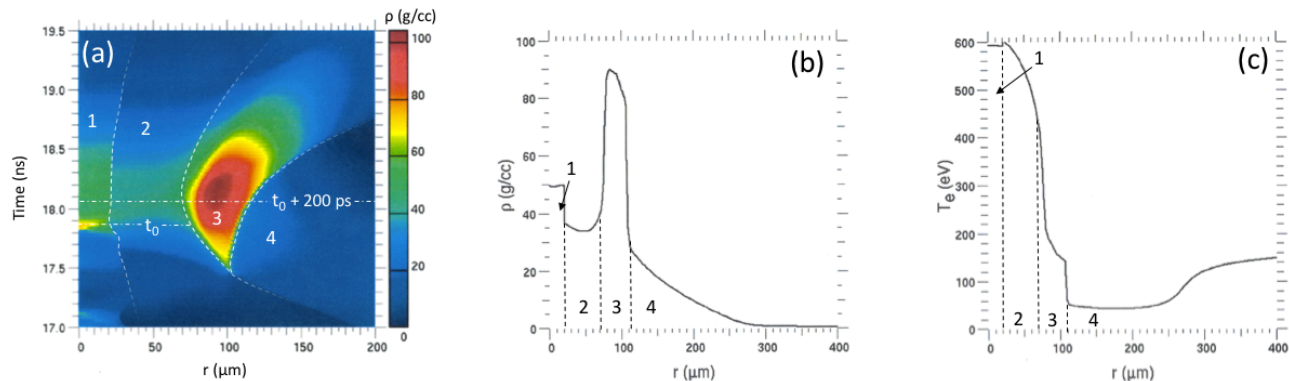


FIG. 4. (a) Spatio-temporal mass density distribution (color-coded, in g/cm^3) from 1D hydro simulations fitted to experimental observables of experiment N160801-001. Time of peak x-ray emission, t_0 , and $t_0 + 200$ ps are denoted by horizontal dash-dotted lines. Radial density (b) and temperature (c) profiles are shown for $t = t_0 + 200$ ps. Different materials are denoted as (1) air core, (2) plastic mandrel, (3) stagnated Be and (4) in-falling Be and ablated material. The air-filled core has a radius of $20 \mu\text{m}$ that plastic layer extends to $70 \mu\text{m}$. Temperatures exceeding 500 eV are predicted out to $55 \mu\text{m}$. In (a), the dashed material boundary lines fade to indicate uncertainty of the constituent locations more than 0.5 ns before and after t_0 .

tegrated area of this curve (cf. Fig. 3(b)), we find that emission time histories relative to t_0 are consistent between shots, regardless of t_0 (cf. Table I). Furthermore, we see that the shape of the emission time histories remains similar between the cone- and stalk-supported capsules, indicating equivalent implosion dynamics between shots. These similarities between shots suggest that a more robust time history of emission can be constructed by aligning the individual time histories relative to their respective peak emission and normalizing the signal intensity. The resulting dataset can be approximated by a two-sided Lorentzian function $L(t - t_0)$, given by

$$L(t - t_0) = \begin{cases} \frac{(\Gamma_l/2)^2}{(t-t_0)^2 + (\Gamma_l/2)^2} & t - t_0 \leq 0 \\ \frac{(\Gamma_r/2)^2}{(t-t_0)^2 + (\Gamma_r/2)^2} & t - t_0 > 0 \end{cases} \quad (1)$$

with centroid t_0 and full-width at half-maxima (FWHM) of the left and right wings Γ_l and Γ_r , respectively. The function is normalized such that $L(0) = 1$.

The FWHM $(\Gamma_l + \Gamma_r)/2$ of the emission feature is found to be $0.38 \pm 0.04 \text{ ns}$ (cf. Fig. 3). Although the measured signal is a convolution of the x-ray emission and the gate pulse of the GXD, the time width of the gate pulse (0.1 ns) is sufficiently shorter than that of the emission to be considered negligible.

Comparison with 1D hydrodynamic simulations (cf. Fig. 4(a)) suggests that the measured time of peak x-ray emission is when the air core reaches maximum density. We note that the experimentally measured emission time history is in excellent agreement with hydrodynamic simulations. As denoted by region 3 in Fig. 4(a), the Be shell starts stagnating at 17.5 ns , and over the next nanosecond keeps aggregating at densities above 50 g/cm^3 . In the simulations, the lower-density tail of in-falling Be is minimized between 500 to 800 ps after peak x-ray emission. Because the simulations predict only moder-

ate mass density variations and a lack of x-ray hot spot emission, the simulations indicate promising conditions for future XRTS studies of dense Be.

As a proof-of-principle exercise, we use the data from experiment N170215-001 to discuss how differential filtering with 1-mm-thick polyimide can be used to infer the hot spot electron temperature, T_{hs} . For this experiment, we find a signal ratio of 0.12 ± 0.015 between the two imaging channels at peak x-ray emission. The biggest uncertainty when inferring T_{hs} comes from uncertainties in the attenuation by the compressed capsule. At peak x-ray emission ($t = t_0$), our hydrodynamic simulations show mass areal densities of $0.135 \pm 0.01 \text{ g/cm}^2$ and $0.37 \pm 0.02 \text{ g/cm}^2$ for the CH layer and the Be capsule, respectively. Furthermore, the impact of Be and C K-shell ionization has to be taken into account, which reduces the opacity if present. Our simulations predict that Be is ionized on average to $Z_{\text{Be}} = 3$ (reducing opacity by $\sim 2x$ compared to cold opacity), and the carbon in the plastic layer to $Z_{\text{C}} = 4.65$ (reducing opacity by $\sim 30\%$ compared to cold opacity).

Based on these assumptions, Figure 5(a) shows the resulting T_{hs} sensitivity as a function of the signal ratio in the two imaging channels. Here, the colored band illustrates the uncertainty of inferring the temperature ($\sim \pm 10\%$), which is dominated by the uncertainty of the shell attenuation as discussed above. The uncertainty in the channel ratio measurement illustrated by the two vertical dashed lines then translates to a range of temperatures of $T_{hs} = 520 \pm 80 \text{ eV}$, which is in good agreement with the predictions of hydrodynamic simulations (cf. Fig. 4(a)). Figure 5(b) shows the corresponding photon spectra that are detected in the two imaging channels. For the inferred hot spot temperature the mean channel energies are $|E_1| = 5450 \text{ eV}$ and $|E_2| = 6425 \text{ eV}$. We note that the error in the channel ratio as shown in Figure 5(a) is rather large due to an unexpected background signal

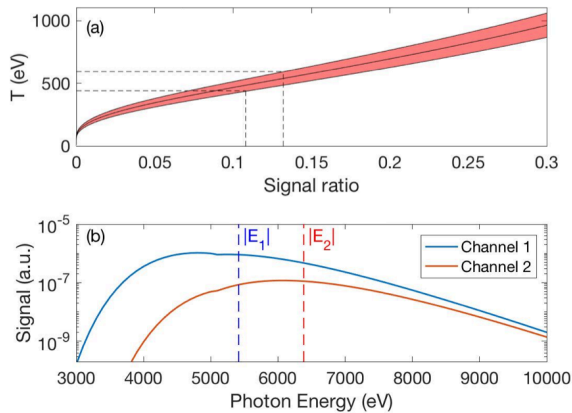


FIG. 5. (a) Temperature as a function of the x-ray emission signal ratio between channels 1 & 2; error range due to uncertainty in capsule shell attenuation. (b) Spectral sensitivity curves for the two imaging channels for $T_{hs} = 520$ eV, inferred from (a). The spectra include corrections for attenuation by the compressed shell and by the installed snout filters, and for the spectral response of the detector. Mean energies are $|E_1| = 5450$ eV and $|E_2| = 6425$ eV.

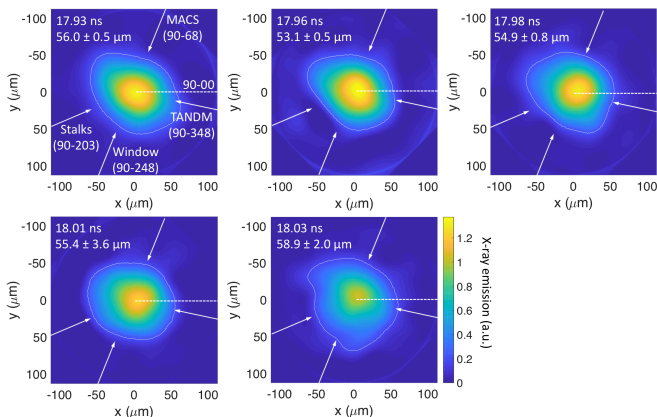


FIG. 6. Sequence of polar-view time-resolved hot spot x-ray images from N171107-001 near $t=t_0$, reconstructed from the measured penumbra. Images are shown with same colormap and smoothed to $20 \mu\text{m}$ spatial resolution. The average radii M_0 , extracted from the 17% contours, are calculated from Legendre mode deconstruction. The directions of the support stalks and the windows (towards and opposite to MACS) are shown because they constitute possible sources of symmetry perturbations. The direction of the target positioner (TANDM) is noted for completeness.

spoil the measurement. The accuracy will be significantly improved on future experiments, translating to a reduced uncertainty in the temperature measurement.

Figure 6 demonstrates that the signal-to-noise of the time-resolved penumbral images recorded with a gated MCP detector is sufficient to enable full spatial reconstruction of the hot-spot shape. The penumbral analysis¹¹ indicates a mostly round emitting region of ra-

dius $M_0 = 55 \pm 3 \mu\text{m}$ with only a very small perturbation in the direction of the support stalks. For all images, almost all higher order Legendre modes remain below 10% of M_0 . The measured M_0 is significantly larger than the core size formed from the original air gas fill of $\sim 20 \mu\text{m}$ (cf. Fig. 4(b)). Some increase in apparent M_0 is expected (simulations predict $M_0 = 43 \mu\text{m}$) since the inner part of the plastic layer is heated to similar temperatures as the gas fill. The additional discrepancy could be due to the finite ($\sim 20 \mu\text{m}$) spatial resolution and possibly because of a slightly oblate implosion.²²

V. CONCLUSION

We have developed and fielded a new x-ray penumbral imaging snout for low hot spot emission capsule implosion experiments at the NIF. For a series of Be implosions, we report similar x-ray emission time histories, which are slightly asymmetric with respect to peak x-ray emission. This consistency enables use of the hot spot x-ray emission as a timing fiducial and accounting for shot-to-shot variations in implosion trajectory. Using differential filtering we infer a hot spot temperature of 520 ± 80 eV for experiment N170215-001, which is consistent with predictions from 1D hydrodynamic simulations. The reconstructed polar-view x-ray hot spot images are close to round with $M_0 = 55 \pm 3 \mu\text{m}$. Hydrodynamic simulations show that peak x-ray emission occurs 0.6 ns prior to the presence of maximum Be shell ρR .

ACKNOWLEDGMENTS

This work was performed under the auspices of the U.S. Department of Energy by Lawrence Livermore National Laboratory under Contract DE-AC52-07NA27344 and supported by Laboratory Directed Research and Development (LDRD) Grant No. 18-ERD-033. M.B., R.R. and B.W. thank the Deutsche Forschungsgemeinschaft (DFG) for support within the Research Unit FOR 2440. D. K. acknowledges support from the Helmholtz Association IVF Grant No. VH-NG-1141.

- ¹E. I. Moses *et al.*, Phys. Plasmas **16**, 041006 (2009).
- ²O. A. Hurricane *et al.*, Nature **506**, 343 (2014).
- ³D. Riley *et al.*, Plasma Phys. Control. Fusion **60**, 014033 (2018).
- ⁴N. Nettelmann *et al.*, Astrophys. J. **750**, 52 (2012).
- ⁵A. Becker *et al.*, Astrophys. J. Suppl. Ser. **215**, 21 (2014).
- ⁶S. H. Glenzer and R. Redmer, Rev. Mod. Phys. **81**, 1625 (2009).
- ⁷D. Kraus, *et al.*, J. Phys. Conf. Ser. **717**, 012067 (2016).
- ⁸D. Kraus *et al.*, Phys. Rev. E **94**, 011202 (2016).
- ⁹T. Döppner *et al.*, Rev. Sci. Instrum. **85**, 11D617 (2014).
- ¹⁰B. Bachmann *et al.*, Rev. Sci. Instrum. **85**, 11D614 (2014).
- ¹¹B. Bachmann *et al.*, Rev. Sci. Instrum. **87**, 11E201 (2016).
- ¹²B. Bachmann *et al.*, Proc. SPIE, Vol. 10390, 103900B (2017).
- ¹³S. A. Letts *et al.*, J. Vac. Sci. Technol. **19**, 739 (1981).
- ¹⁴A. Saunders *et al.*, High Energy Density Phys. **26** 86 (2018).
- ¹⁵J. L. Kline *et al.*, Physics of Plasmas **23**, 056310 (2016).
- ¹⁶V. A. Smalyuk *et al.*, Phys. Rev. Lett. **112**, 185003 (2014).
- ¹⁷K. S. Raman *et al.*, Physics of Plasmas **21**, 072710 (2014).

¹⁸J. A. Oertel *et al.*, Rev. Sci. Instrum. **77**, 10E308 (2006).

¹⁹J. R. Kimbrough *et al.*, Rev. Sci. Instrum. **81**, 10E530 (2010).

²⁰L. R. Benedetti *et al.*, Rev. Sci. Instrum. **87**, 023511 (2016).

²¹B. Bachmann *et al.*, J. Phys. D **46**, 125203 (2013).

²²While complementary equatorial radiography measurements showed a round implosion, it is well-known that equatorial shape can change as function of laser delivery into the hohlraum.